Contents lists available at ScienceDirect

Journal of Rock Mechanics and Geotechnical Engineering

Full Length Article

A stable implicit nodal integration-based particle finite element method (N-PFEM) for modelling saturated soil dynamics

Liang Wang [a], Xue Zhang [b,*], Jingjing Meng [c], Qinghua Lei [a,d]

[a] *Department of Earth Sciences, ETH Zürich, Zürich, 8092, Switzerland*
[b] *Department of Civil Engineering and Industrial Design, University of Liverpool, Liverpool, L69 3BX, UK*
[c] *Department of Civil, Environmental and Natural Resources Engineering, Luleå University of Technology, Luleå, 97187, Sweden*
[d] *Department of Earth Sciences, Uppsala University, Uppsala, 75105, Sweden*

ARTICLE INFO

ABSTRACT

In this study, we present a novel nodal integration-based particle finite element method (N-PFEM) designed for the dynamic analysis of saturated soils. Our approach incorporates the nodal integration technique into a generalised Hellinger-Reissner (HR) variational principle, creating an implicit PFEM formulation. To mitigate the volumetric locking issue in low-order elements, we employ a node-based strain smoothing technique. By discretising field variables at the centre of smoothing cells, we achieve nodal integration over cells, eliminating the need for sophisticated mapping operations after re-meshing in the PFEM. We express the discretised governing equations as a min-max optimisation problem, which is further reformulated as a standard second-order cone programming (SOCP) problem. Stresses, pore water pressure, and displacements are simultaneously determined using the advanced primal-dual interior point method. Consequently, our numerical model offers improved accuracy for stresses and pore water pressure compared to the displacement-based PFEM formulation. Numerical experiments demonstrate that the N-PFEM efficiently captures both transient and long-term hydro-mechanical behaviour of saturated soils with high accuracy, obviating the need for stabilisation or regularisation techniques commonly employed in other nodal integration-based PFEM approaches. This work holds significant implications for the development of robust and accurate numerical tools for studying saturated soil dynamics.

© 2024 Institute of Rock and Soil Mechanics, Chinese Academy of Sciences. Production and hosting by Elsevier B.V. This is an open access article under the CC BY license (http://creativecommons.org/licenses/by/4.0/).

1. Introduction

Saturated soil represents a multiphase material comprising a solid skeleton and fluid occupying voids. The study of saturated soil dynamics has long been recognised as a challenging problem (Zienkiewicz and Shiomi, 1984), necessitating the simultaneous analysis of both solid and fluid phases and their interactions (Zienkiewicz et al., 1980). Time-dependent processes in saturated soils (Bjerrum, 1967; Olson, 1998), such as soil consolidation and the dissipation of pore water pressure, introduce additional complexity for numerical modelling. This complexity arises from the need for numerical schemes with appropriate time-stepping and convergence criteria (Prevost, 1983; Zienkiewicz et al., 1999).

In situations where soils undergo significant deformation, as observed in landslides and foundation penetration processes, numerical modelling becomes even more challenging. This is due to potential issues related to mesh distortion and the evolution of free-surfaces.

Over the past decades, significant advances have been made in the development of numerical methods for modelling saturated soil dynamics under large deformation. These methods include the Arbitrary Lagrangian-Eulerian method (Sabetamal et al., 2014), Smoothed Particle Hydrodynamics method (Pastor et al., 2009; Bui and Nguyen, 2017; Peng et al., 2017), Material Point Method (Zhang et al., 2009; Bandara and Soga, 2015; Yamaguchi et al., 2020; Kularathna et al., 2021), and the Particle Finite Element Method (PFEM) (Monforte et al., 2019; Wang et al., 2021a; Carbonell et al., 2022; Jin and Yin, 2022), among others. In these studies, the coupling between the solid skeleton and the pore fluid is described through either the Biot formulation in a set of governing equations for the solid-fluid mixture (Zienkiewicz and Shiomi, 1984) or

---

* Corresponding author.
  E-mail address: xue.zhang2@liverpool.ac.uk (X. Zhang).
  Peer review under responsibility of Institute of Rock and Soil Mechanics, Chinese Academy of Sciences.

through models of interaction forces added to two separate sets of governing equations for the two phases (Drew, 1983). Due to its effectiveness and efficiency, the Biot formulation has been widely adopted in the development of these methods for various practical applications (Pastor et al., 2009; Zhang et al., 2009; Monforte et al., 2019; Wang et al., 2021a; Jin and Yin, 2022). While interaction models can capture more complex coupling processes between two-phase materials, the computational cost is higher since the solid and fluid phases are separately simulated (Bandara and Soga, 2015; Bui and Nguyen, 2017). Among these developments, explicit time integration schemes with conditional stability are most commonly used, although they are not computationally efficient for analysing geotechnical problems characterised by low to medium frequency. Recently, semi-implicit and implicit time integration schemes have been implemented in these methods to improve the computational efficiency (Kularathna et al., 2021; Wang et al., 2021a; Carbonell et al., 2022; Lian et al., 2023).

The PFEM is a hybrid method that combines finite element analysis with the feature of particle approaches. Originally developed in the fluid dynamics community to model free-surface flow and fluid-structure interaction problems (Oñate et al., 2004), the PFEM has gradually gained recognition in geotechnical community as well. Various versions of the PFEM have been developed to tackle large deformation problems in geotechnical engineering applications. The PFEM has become popular due to its two key features: (i) it naturally inherits the demonstrated capability of the FEM in describing the complex nonlinear behaviour of geomaterials, and (ii) pre-existing FEM codes can be easily extended to incorporate the particle technique (Oñate et al., 2004; Cremonesi et al., 2011; Zhang et al., 2013) for large deformation analysis.

Among recent PFEM developments, one important improvement is the adoption of a nodal integration scheme (Zhang et al., 2018). This scheme eliminates the mapping requirement after the re-meshing operation in modelling history-dependent materials, as all state variables are stored at mesh nodes. Remarkably, in most developed nodal integration-based PFEM versions, it has been shown that numerical instabilities may arise in the dynamic analysis of both single-phase (Jin et al., 2021a; Yuan et al., 2023a) and two-phase materials (Jin and Yin, 2022; Wang et al., 2023a; Yuan et al., 2023b) if no stabilisation technique is imposed. For single-phase materials, instability arises from low-order integration, known as temporal instability, which has also been observed in nodal integration-based smoothed FEM (Zhang and Liu, 2010) and various other mesh-free methods (Belytschko et al., 2000; Chen et al., 2001). Concerning two-phase materials, the additional inf-sup condition (Franco and Bathe, 1990) should be fulfilled since equal order shape functions are used. The introduction of stabilisation may involve different techniques or tunable parameters for multiple problems, for which no universal criteria are available (Belytschko et al., 2000; Puso et al., 2008; Silva-Valenzuela et al., 2020; Wei et al., 2020). Furthermore, in some developed nodal integration-based PFEM versions (Jin and Yin, 2022; Yuan et al., 2022), explicit or semi-implicit schemes were adopted, which may be less efficient in simulating long-term geotechnical problems, such as consolidation settlement in clay.

To circumvent the use of stabilisation techniques and develop an implicit PFEM version, the second-order cone programming (SOCP) is considered as a promising solution. The adoption of mixed variational principles, consolidating all the governing equations into a single functional, can achieve better accuracy in stress calculation, compared to displacement-based FEM (Reddy, 2002). Previous studies have demonstrated that an accurate and efficient implicit time integration scheme is compatible with the SOCP-based computational framework (Zhang et al., 2013, 2019, 2023; Wang et al., 2021a, 2023b; Wang and Lei, 2023). Recently, the

temporal stability of an implicit nodal integration-based PFEM (N-PFEM) using SOCP has been validated for dynamic total stress analysis of single-phase materials (Zhang et al., 2023), and in the dynamic effective stress analysis of saturated media (Wang et al., 2023c) without the need for *ad-hoc* stabilisation techniques. However, the N-PFEM proposed in the work of Wang et al. (2023c) is limited to simulating saturated soils in two extreme conditions, i.e., fully undrained and fully drained circumstances. In other words, it can only be applied to the limiting scenarios, i.e., short-term analyses of saturated soils with very low permeability and long-term analyses where excess pore water pressure is fully dissipated. It cannot capture water transport in porous media and its sequential effects on soil deformation. Water transport plays an important role in many geotechnical problems. One example is soil consolidation settlement. Another noteworthy scenario involves the initiation of catastrophic failure, exemplified by the determination of the timing and mechanisms of landslides (Iverson et al., 1997; Torres et al., 1998; Berti and Simoni, 2005).

In this study, we further extend the N-PFEM for the coupled dynamic analysis of saturated media, considering water seepage. This development is based on the generalised Hellinger-Reissner (HR) variational principle as proposed in the work of Wang et al. (2021a). The coupled N-PFEM developed in this study is assessed by studying a range of challenging geotechnical problems, such as wave propagation, strip footing, and consolidation, which require the fulfilments of temporal stability and the inf-sup condition. It is demonstrated that, while inheriting the advantages of the conventional nodal integration-based PFEM for modelling large deformation problems, the developed N-PFEM also successfully reproduces smooth effective stress and pore water pressure fields without the need for any stabilisation technique.

2. Model description

In this section, the governing equations and solution schemes of the current numerical model are briefly introduced. More theoretical and technical details can be found in our previous studies (Zhang et al., 2013, 2019, 2022; Wang et al., 2021a,b).

2.1. Governing equations

A two-dimensional (2D) domain, *V*, comprising saturated porous media and bounded by a surface *S*, is considered, as shown in Fig. 1.

The governing equations for dynamic saturated media are below (Zienkiewicz et al., 1999; De Boer, 2012):
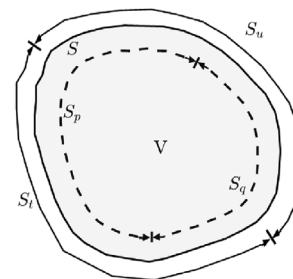
(a) The equilibrium equation for the mixture

Fig. 1. Domain of a saturated medium and its boundary partition. S_t, S_u, S_p and S_q represent the associated surfaces subjected to traction, displacement, pore water pressure, and fluid flux, respectively.

$$\nabla^T(\sigma' + mp) + b = \rho\dot{v} \quad (\text{in } V) \tag{1}$$

where σ' is the effective stress; m is the vector, $m = [1,1,0]$; p is the pore water pressure; b is the body force; ρ is the density; ∇ is the linear strain-displacement operator; and v is the velocity.

(b) Displacement-strain relation

$$\varepsilon = \nabla u \tag{2}$$

where ε is the strain and u is the displacement.

(c) Darcy's law

$$\nabla p + b_f - \frac{\gamma_f}{k} w = \rho_f \dot{v} \tag{3}$$

where ρ_f, γ_f, and b_f are the density, the unit weight, and the body force of a fluid, respectively; k is the Darcy hydraulic conductivity; and w is the superficial velocity.

(d) Mass balance equation

$$\nabla^T w + \nabla^T v = 0 \tag{4}$$

where w can be eliminated by substituting Eq. (3) into Eq. (4):

$$\nabla^T \frac{k}{\gamma_f} \left(\nabla p + b_f - \rho_f \dot{v} \right) + \nabla^T v = 0 \tag{5}$$

(e) Boundary conditions

$$N^T(\sigma' + mp) = t \quad (\text{on } S_t) \tag{6}$$

$$u = u^p \quad (\text{on } S_u) \tag{7}$$

$$p = p^p \quad (\text{on } S_p) \tag{8}$$

$$N^T \frac{k}{\gamma_f} \left(\nabla p + b_f - \rho_f \dot{v} \right) + \nabla^T v = q^p \quad (\text{on } S_q) \tag{9}$$

where N is a matrix consisting of components of the outward normal vector of the boundary; and t, u^p, p^p and q^p are the prescribed traction, displacement, pore water pressure and fluid flux, respectively.

(f) Constitutive equations of elastoplasticity

$$F(\sigma') \le 0 \tag{10}$$

$$\varepsilon = \varepsilon^e + \varepsilon^p, \ \varepsilon^e = \mathbb{C}\sigma', \ \varepsilon^p = \lambda\nabla G(\sigma') \tag{11}$$

where F is the yield function; ε^e and ε^p are the elastic and plastic strains, respectively; $\mathbb{C}$ is the elastic compliance matrix; λ is the plastic multiplier; and G is the plastic potential. The associated flow rule assumes $G = F$. The incremental forms of Eqs. (10) and (11) with their complementary conditions can be expressed as

$$\left. \begin{array}{l} F(\sigma') \le 0 \\ \Delta\varepsilon = \mathbb{C}\Delta\sigma' + \Delta\lambda\nabla F(\sigma') \\ \Delta\lambda F(\sigma') = 0 \quad (\Delta\lambda \ge 0) \end{array} \right\} \tag{12}$$

The above governing equations are the so-called u-p form suitable for dynamic analysis of geotechnical problems of low to medium frequency (Zienkiewicz et al., 1999). The porosity n can be updated by $\dot{n} = (1 - n)\nabla \cdot v$, assuming the solid skeleton is incompressible (De Boer, 2012). The density of the mixture is calculated as $\rho = n\rho_f + (1-n)\rho_s$, where ρ_s is the density of the solid.

2.2. Time discretisation

Using the θ-method (Wood, 1990), the effective stress, velocity, and pore water pressure are discretised in time as

$$\sigma' = \theta_1\sigma'_{n+1} + (1 - \theta_1)\sigma'_n \tag{13}$$

$$v = \dot{u} = \frac{u_{n+1} - u_n}{\Delta t} = \frac{\Delta u}{\Delta t} = \theta_2 v_{n+1} + (1 - \theta_2)v_n \tag{14}$$

$$p = \theta_3 p_{n+1} + (1 - \theta_3)p_n \tag{15}$$

where the subscripts n and $n+1$ denote the known and unknown states; Δt is the time step; and θ_1, θ_2 and θ_3 are the numerical parameters ranging from 0 to 1. Substituting Eqs (13)–(15) into the equilibrium Eq. (1) and boundary conditions Eqs. (6) and (9) gives

$$\nabla^T\sigma'_{n+1} + \frac{(1-\theta_1)}{\theta_1}\nabla^T\sigma'_n + \frac{\theta_3}{\theta_1}\nabla^T mp_{n+1} + \frac{(1-\theta_3)}{\theta_1}\nabla^T mp_n + \tilde{b} = r_{n+1} \tag{16}$$

$$N^T\left(\sigma'_{n+1} + \frac{\theta_3}{\theta_1}mp_{n+1}\right) = \tilde{t} \tag{17}$$

$$N^T\frac{k\theta_1}{\gamma_f}\left(\frac{\theta_3}{\theta_1}\nabla p_{n+1} + \tilde{b}_f\right) = q^p \tag{18}$$

where

$$\left. \begin{array}{l} \tilde{b} = \frac{1}{\theta_1}b + \tilde{\rho}\frac{v_n}{\Delta t} \\[4pt] \tilde{\rho} = \frac{\rho}{\theta_1\theta_2} \\[4pt] r_{n+1} = \tilde{\rho}\frac{\Delta u}{\Delta t^2} \\[4pt] \tilde{t} = \frac{1}{\theta_1}t - \frac{1-\theta_1}{\theta_1}N^T\sigma'_n - \frac{1-\theta_3}{\theta_1}N^T mp_n \\[4pt] \tilde{b}_f = \frac{1}{\theta_1}b_f + \frac{(1-\theta_3)}{\theta_1}\nabla p_n - \tilde{\rho}_f\dot{v} \\[4pt] \tilde{\rho}_f = \frac{\rho_f}{\theta_1} \end{array} \right\} \tag{19}$$

Wang et al. (2021a) demonstrated that the above time marching

scheme is unconditionally stable for dynamic analysis of saturated media if $\theta_{1,2,3} \geq 0.5$. In this study, we use $\theta_1 = \theta_2 = \theta_3 = 1$ unless otherwise specified.

2.3. Spatial domain discretisation with nodal integration

Three-node triangular elements are adopted for finite element discretisation, with a nodal integration scheme implemented over smoothing cells. This scheme has been demonstrated to be effective in addressing volumetric locking issues associated with linear elements (Zeng and Liu, 2018; Zhang et al., 2018; Meng et al., 2020). Following standard finite element notations, the displacement field $\boldsymbol{u}$ is approximated by

$$\sigma' \approx \overline{\sigma}', \boldsymbol{r} \approx \overline{\boldsymbol{r}}, p \approx \overline{p}, \chi \approx \overline{\chi} \tag{24}$$

where the overbar represents the value over the smoothing cell (also the value at the mesh node associated with this smoothing cell). For brevity, an intermediate variable $\chi = \frac{\theta_3}{\theta_1}\nabla p + \tilde{\boldsymbol{b}}_f$ is introduced (Zhang et al., 2016; Wang et al., 2021a).

2.4. Solution scheme

2.4.1. Optimisation problem

According to the generalised Hellinger-Reissner variational principle proposed by Wang et al. (2021a), the discretised governing equations for saturated soil dynamics are equivalent to the following min-max problem:

$$\min_{\Delta \dot{\boldsymbol{u}}} \max_{(\overline{\sigma}', \overline{\boldsymbol{r}}, \overline{p})_{n+1}} -\frac{1}{2}\Delta\overline{\sigma}'^{\mathrm{T}}\boldsymbol{C}\Delta\overline{\sigma}' + \Delta\widehat{\boldsymbol{u}}^{\mathrm{T}}\boldsymbol{B}^{\mathrm{T}}\left(\overline{\sigma}'_{n+1} + \frac{\theta_3}{\theta_1}\boldsymbol{m}\overline{p}_{n+1}\right) - \Delta\widehat{\boldsymbol{u}}^{\mathrm{T}}\tilde{\boldsymbol{f}} + \Delta\widehat{\boldsymbol{u}}^{\mathrm{T}}\boldsymbol{A}^{\mathrm{T}}\overline{\boldsymbol{r}}_{n+1} - \frac{\Delta t^2}{2}\overline{\boldsymbol{r}}_{n+1}^{\mathrm{T}}\boldsymbol{D}\overline{\boldsymbol{r}}_{n+1} - \frac{\Delta t}{2}\overline{\chi}_{n+1}^{\mathrm{T}}\boldsymbol{K}\overline{\chi}_{n+1} - \Delta t\overline{p}_{n+1}^{\mathrm{T}}\tilde{\boldsymbol{f}}^{q}$$

$$\text{subject to} \quad F(\overline{\sigma}'_{n+1}) \leq 0 \tag{25}$$

$$\boldsymbol{A}\overline{\chi}_{n+1} - \boldsymbol{B}_p\overline{p}_{n+1} = \tilde{\boldsymbol{f}}^{b}$$

$$\boldsymbol{u} \approx \boldsymbol{N}_u\widehat{\boldsymbol{u}} \tag{20}$$

where the hat symbol "ʌ" represents variables at mesh nodes, and $\boldsymbol{N}_u$ is the matrix containing the linear interpolation shape functions. The strain tensor ε over finite elements is then expressed as

$$\left.\begin{array}{l}\varepsilon = \nabla\boldsymbol{u} \approx \boldsymbol{B}_u\widehat{\boldsymbol{u}} \\ \boldsymbol{B}_u = \nabla\boldsymbol{N}_u\end{array}\right\} \tag{21}$$

Due to the linear shape function, the strain tensor ε is uniform within each three-node triangular element. Hence, the smoothed strain at each mesh node can be evaluated as a weighted average of strain over the smoothing cell (Chen et al., 2001; Liu et al., 2007; Zeng and Liu, 2018; Zhang et al., 2018; Meng et al., 2020). As illustrated in Fig. 2, cells are constructed by connecting the centroid of each triangle to its three mid-edge nodes. The smoothed strain at the kth node (or the strain across the kth smoothing cell) is

$$\overline{\varepsilon}_k = 1 \Big/ A_k^s \sum_{i=1}^{N_s} \frac{1}{3}A_i^e\boldsymbol{B}_{u,i}^e\widehat{\boldsymbol{u}}_i^e \tag{22}$$

where A_k^s is the area of the kth smoothing cell Ω_k^s, N_s is the number of elements contributing to the kth smoothing cell, and A_i^e, $\boldsymbol{B}_{u,i}^e$ and $\widehat{\boldsymbol{u}}_i^e$ are respectively the area, strain gradient matrix and nodal displacement of the ith linear triangular element involved in the kth smoothing cell. The relationship between the smoothed strain and nodal displacement at the kth node can be further expressed as (Meng et al., 2020):

$$\overline{\varepsilon}_k = \overline{\boldsymbol{B}}_k\widehat{\boldsymbol{u}}_k, \tag{23}$$

with $\overline{\boldsymbol{B}}_k = (1/A_k^s)\sum_{i=1}^{N_s}\frac{1}{3}A_i^e\boldsymbol{B}_{u,i}^e$ being the smoothed strain gradient matrix.

Other master fields, such as the effective stress σ', the pore water pressure p, and the dynamic force $\boldsymbol{r}$, are also assumed uniform across each smoothing cell

The equivalence between this min-max problem and the governing equations can be verified by taking functional derivatives of the associated Lagrangian functional (Wang et al., 2021a), as shown in Appendix A. However, it is noteworthy that, in this study, all the matrices in the min-max problem (25) are calculated over smoothing cells, which differs from those in the work of Wang et al. (2021a), where they were estimated on finite elements. This difference arises due to the utilisation of nodal integration in this study. Specifically, the matrices and vectors in the min-max problem (25) are

$$\left.\begin{array}{l}\boldsymbol{C} = \displaystyle\int_{\Omega^s}\mathbb{C}\mathrm{d}\Omega \\[8pt] \boldsymbol{B}^{\mathrm{T}} = \displaystyle\int_{\Omega^s}(\overline{\boldsymbol{B}}_k)^{\mathrm{T}}\mathrm{d}\Omega \\[8pt] \boldsymbol{A}^{\mathrm{T}} = \displaystyle\int_{\Omega^s}\boldsymbol{I}\mathrm{d}\Omega \\[8pt] \boldsymbol{D} = \displaystyle\int_{\Omega^s}\tilde{\rho}^{-1}\mathrm{d}\Omega \\[8pt] \boldsymbol{K} = \displaystyle\int_{\Omega^s}\frac{k\theta_1}{\gamma_f}\mathrm{d}\Omega \\[8pt] \boldsymbol{B}_p = \dfrac{\theta_3}{\theta_1}\displaystyle\int_{\Omega^s}(\overline{\boldsymbol{B}}_k)^{\mathrm{T}}\mathrm{d}\Omega \\[8pt] \tilde{\boldsymbol{f}}^{b} = \displaystyle\int_{\Omega^s}\tilde{\boldsymbol{b}}_f\mathrm{d}\Omega \\[8pt] \boldsymbol{f}^{q} = \dfrac{\theta_3}{\theta_1}\displaystyle\int_{\Gamma^s}q^p\mathrm{d}\Gamma \\[8pt] \tilde{\boldsymbol{f}} = \displaystyle\int_{\Omega^s}\tilde{\boldsymbol{b}}\mathrm{d}\Omega + \int_{\Gamma^s}\frac{1}{\theta_1}\boldsymbol{t}\mathrm{d}\Gamma - \frac{(1-\theta_1)}{\theta_1}\boldsymbol{B}^{\mathrm{T}}\overline{\sigma}_n - \frac{(1-\theta_3)}{\theta_1}\boldsymbol{B}^{\mathrm{T}}\boldsymbol{m}\overline{p}_n\end{array}\right\}$$

$$\tag{26}$$

where $\boldsymbol{I}$ is an identity matrix, and Ω^s is the smoothing cell.
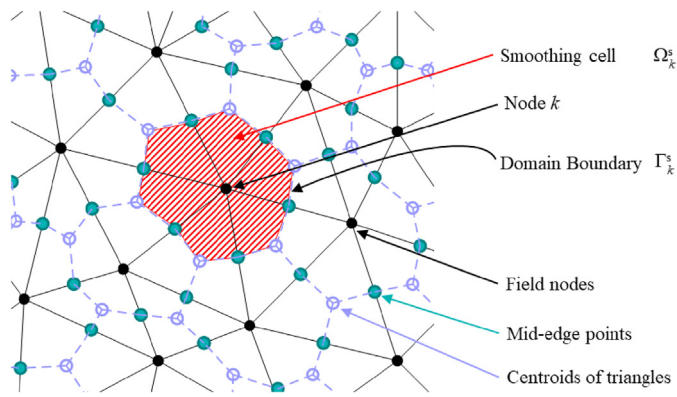
Fig. 2. Schematic of node-based smoothing cells created based on adjacent triangular elements. Each smoothing cell consists of N_s sub-cells and each sub-cell is one-third of the corresponding linear triangular element.

The min-max problem (25) can be further reformulated as a standard SOCP problem with different yield criteria, such as Tresca, Mohr−Coulomb and Drucker-Prager functions (Zhang et al., 2013, 2019), and the implementation details have been documented by Wang et al. (2021b). In Appendix B, the reformulated SOCP problem is presented.

2.4.2. N-PFEM

The PFEM treats mesh nodes as free particles within the framework of Lagrangian FEM. The evolving computational domain is identified using the alpha-shape method (Edelsbrunner and Mücke, 1994; Oñate et al., 2004; Cremonesi et al., 2010): for a cloud of points with a characteristic length h, an examination is performed on each point to check whether it is possible to place a sphere with a radius αh (α is a pre-defined factor usually varying from 1.2 to 1.6) such that it only contains that point; if possible, the point is a boundary point; otherwise, it is an internal point. During the PFEM simulation, the boundary of the computational domain associated with a new mesh is obtained by removing unnecessary elements from the mesh generated through Delaunay triangulation of updated mesh nodes (Cremonesi et al., 2010). However, the quality of the resulting mesh is usually insufficient for classical FEM analysis to handle large deformation. Therefore, a re-meshing or mesh smoothing operation on the identified domain is needed to ensure mesh quality (Zhang et al., 2013; Cante et al., 2014; Meduri et al., 2019; Wang et al., 2022). Alternatively, the smoothing technique employed in smoothed finite element methods can alleviate

Fig. 3. Schematic of the N-PFEM calculation procedures from time step n to $n+1$: (a) a cloud of particles at t_n; (b) triangular elements obtained from the alpha-shape method at t_n; (c) constructed node-based smoothing cells at t_n; and (d) updated particle positions at t_{n+1}.

this issue by using cells rather than finite elements for spatial domain discretisation (Yuan et al., 2019; Zhang et al., 2018, 2021, 2022).

In this paper, a nodal integration scheme is introduced into PFEM for poro-elastoplastic analysis of saturated porous media. The basic calculation procedures of the developed N-PFEM within each time step are as follows:

(i) A cloud of particles (vertices) is used to represent the computational domain (Fig. 3a);
(ii) The alpha-shape method is employed to identify the computational domain, which also generates a new mesh through Delaunay triangulation (Fig. 3b);
(iii) Smoothing cells are constructed for each node of triangular elements (Fig. 3c);
(iv) Incremental finite element analysis is performed;
(v) Field variables at all nodes are updated (e.g. the coordinates of particles are updated using the resolved incremental displacements, as shown in Fig. 3d).

In procedure (ii), mesh refinements, involving actions such as node deletion and insertion, are necessary to ensure a high-quality mesh, as indicated by Meduri et al. (2019). These measures are particularly essential when addressing situations with profound deformations, such as those observed in flow-like landslides, breaking waves, and splashes. Additionally, there is the possibility of introducing additional nodes to enhance the precision of numerical simulation. It is worth noting that these refinements could potentially lead to a modification in the total number of nodes, necessitating variable mapping procedures for the newly added nodes.

In the proposed N-PFEM, we adopt the infinitesimal strain (Eq. (2)) with an updated geometry for large deformation analysis. The use of infinitesimal strain for large deformation analysis has proven to be effective in geotechnical applications (Hu and Randolph, 1998; Tian et al., 2014; Wang et al., 2015; Kong et al., 2018). Notably, the PFEM with this strategy has demonstrated its effectiveness in reproducing large deformational phenomena observed in laboratory experiments. Examples include water dam break flow (Zhang et al., 2019), dry (Zhang et al., 2014) and saturated (Wang et al., 2021a) granular collapses, and submarine landslide-generated waves (Zhang et al., 2019, 2022). In these cases, good agreements were achieved between numerical simulations and experimental measurements. Its effectiveness will be further demonstrated for dealing with saturated soil under large deformation through several benchmarks to be presented in Section 3.

3. Numerical examples

To validate and demonstrate the proposed model for dynamic analysis of saturated media, numerical simulations are conducted for four benchmarks. These benchmarks cover both elastic and elastoplastic scenarios as well as both small and large deformations. The first two examples involve simulations where node positions are not updated, representing small deformation cases. In contrast, the third and fourth examples utilise the complete N-PFEM procedures, as outlined in Section 2.4.2, to perform the large deformation analysis.

3.1. Wave propagation

In this example, we study a typical benchmark for the dynamic analysis of saturated media (Markert et al., 2010): the wave propagation in a 2D rectangular saturated weightless poroelastic medium. The model setup is shown in Fig. 4a, where a surface load
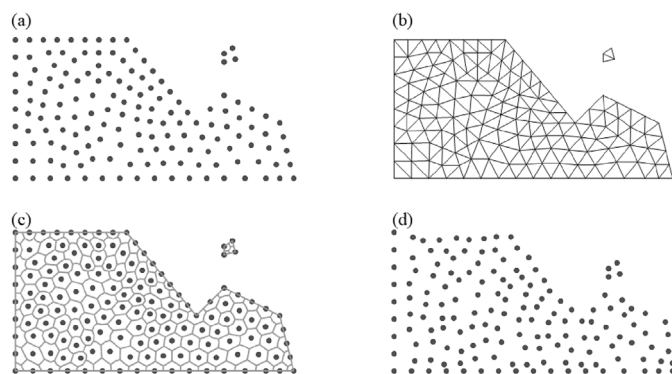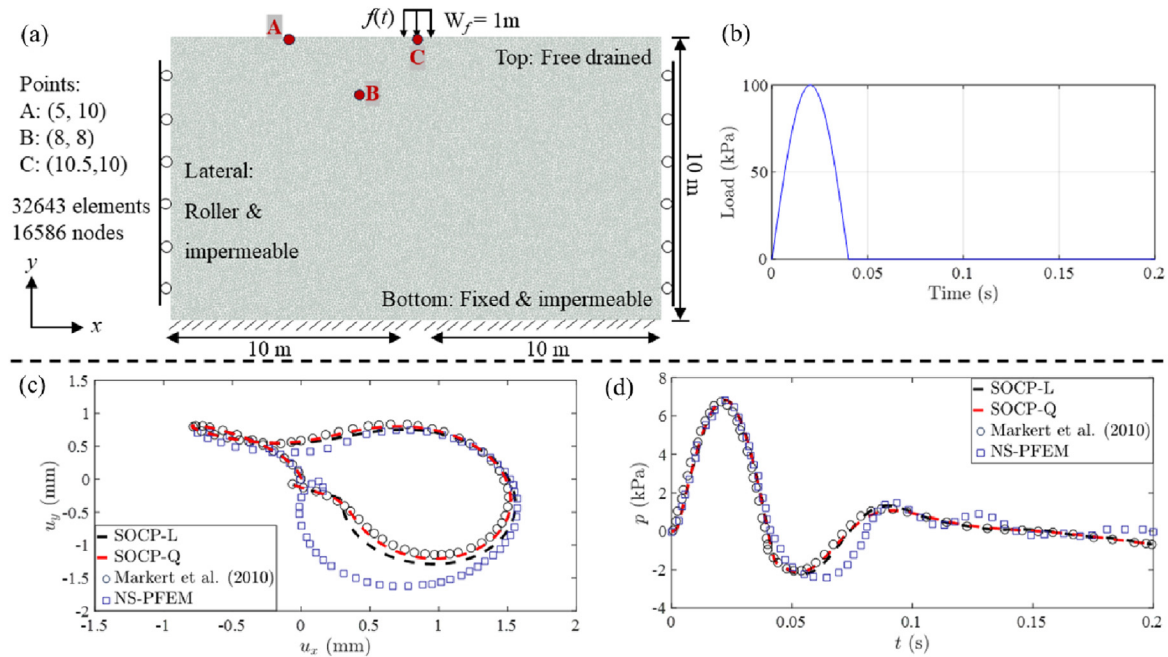
Fig. 4. Wave propagation in a 2D saturated weightless poroelastic medium: (a) model setup; (b) time-load function; (c) displacement at point A compared with results of Markert et al. (2010) and the NS-PFEM results (Wang et al., 2023a); and (d) pressure at point B compared with results of Markert et al. (2010) and the NS-PFEM results (Wang et al., 2023a).

with a width $W_f = 1$ m is applied at the top surface of the domain. The load obeys the function $f(t) = 100\sin(25\pi t)(1-H(t\text{-}0.04))$ kPa, where H denotes the Heaviside step function, and lasts for 0.04 s (Fig. 4b). Material parameters used in this study are the same as those in the work of Markert et al. (2010): the density of solid $\rho_s = 2000$ kg/m^3, the density of fluid $\rho_f = 1000$ kg/m^3, porosity $n = 0.33$, Young's modulus $E = 14.5$ MPa, Poisson's ratio $\nu = 0.3$, and the Darcy hydraulic conductivity $k = 10^{-2}$ m/s. The computational domain is discretised using 16,586 nodes and 32,643 three-node triangular elements, based on which 16,586 smoothing cells are constructed. The time step adopted in the simulation is 0.005 s, facilitating an accurate representation of wave propagation over a duration of 0.2 s. Consequently, a total of 400 simulation steps are executed.

Fig. 4c and d presents the evolution history of the displacement at point A and the pressure at point B obtained from our simulation (SOCP-L). These results are also compared with the reference solutions from the work of Markert et al. (2010), the standard nodal integration-based smoothed PFEM without stabilisation techniques from the work of Wang et al. (2023a) (denoted as NS-PFEM), and the simulation results obtained from the same SOCP-based FE computational framework reported by Wang et al. (2021a) using quadratic displacement/linear stress mixed elements (SOCP-Q). Satisfactory agreements are observed between SOCP-Q, SOCP-L, and the results of Markert et al. (2010), demonstrating the accuracy of the proposed nodal integration scheme for the dynamic analysis of saturated media. As for the NS-PFEM, incorrect results (i.e. wrong shape of the displacement at A and the oscillation of pore water pressure at B) are obtained due to the temporal instability-induced non-physical oscillations, as reported by Wang et al. (2023a). The slight discrepancy in the displacement obtained from SOCP-L, as compared to SOCP-Q and the results from the work of Markert et al. (2010), can be attributed to the utilisation of shape functions one order lower in the current method. It is worth noting that SOCP-Q (Wang et al., 2021a) employs quadratic/linear mixed triangular elements, resulting in a higher number of mesh nodes (i.e. 65,814). Consequently, SOCP-Q exhibits lower computational efficiency

compared to the nodal integration-based method developed in our study (i.e. SOCP-L). This is evident from the computational times of 240 min for SOCP-L and 759 min for SOCP-Q in solving this benchmark problem, using a Windows 10 Desktop with an Intel i7 CPU @ 3.00 GHz.

To further demonstrate the numerical stability of our proposed method for dynamic analysis of saturated media, wavefields of pore water pressure at $t = 0.05$ s are illustrated in Fig. 5, where the displacement is scaled by a factor of 250. The simulation results obtained from the developed SOCP-based method using linear elements and nodal integration (referred to as SOCP-L) are compared with those from the conventional FE simulation using linear elements, both with and without stabilisation as described by Monforte et al. (2019). As can be seen, unphysical oscillation is present in the conventional FE simulation results when linear elements are used without stabilisation techniques (Fig. 5c). In contrast, our method demonstrates the ability to generate a smooth wavefield, as depicted in Fig. 5a, even in the absence of any stabilisation techniques on linear elements. While for the simulation of this problem using the NS-PFEM model (Wang et al., 2023a), severe numerical noises related to temporal instability are observed if stabilisation techniques are not applied. Notably, the results obtained from our method exhibit good agreement with those using the same SOCP-based formulation with quadratic/linear mixed elements (Fig. 5b) and conventional FE simulation with stabilisation techniques (Fig. 5d).

3.2. Strip footing and long-term consolidation

In this section, the long-term consolidation of both elastic and elastoplastic saturated soil subjected to footing under small deformations is considered. This problem has also been examined in various previous studies (Jin et al., 2021b; Yuan et al., 2023b). The model setup is as shown in Fig. 6a, consistent with those in the work of Manoharan and Dasgupta (1995) and Yuan et al. (2023b). Material parameters are as follows: the density of solid $\rho_s = 2000$ kg/m^3, the density of fluid $\rho_f = 1000$ kg/m^3, porosity
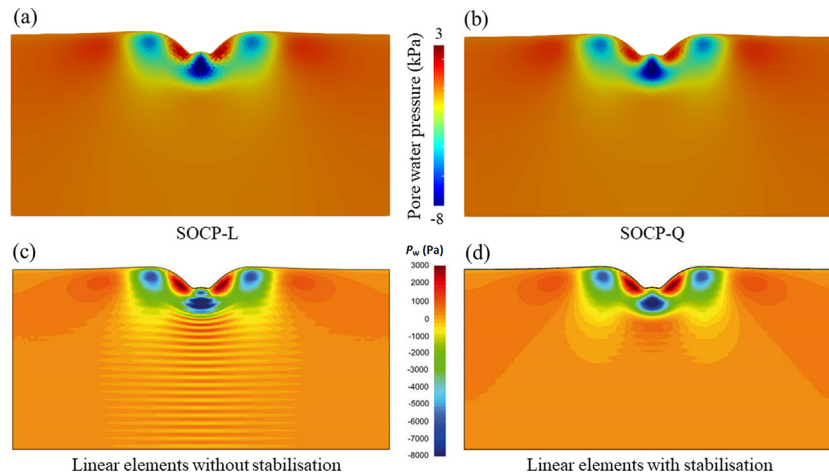
Fig. 5. Wavefields of pore water pressure at $t = 0.05$ s calculated by: (a) our nodal integration-based SOCP-L and (b) SOCP-Q methods, in comparison to (c) the conventional FE with linear elements without stabilisation (Monforte et al., 2019) and (d) with stabilisation (Monforte et al., 2019). The displacement field is scaled by a factor of 250.
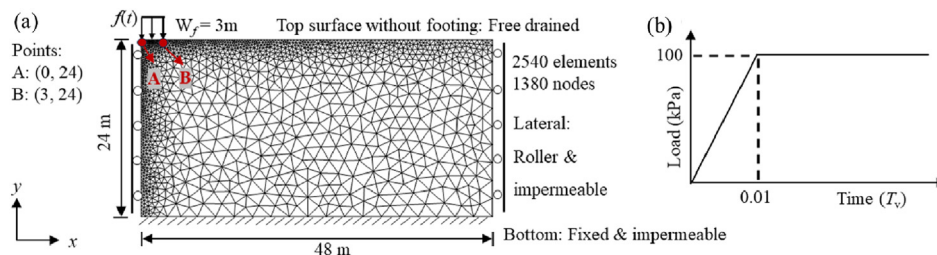

Fig. 6. Strip footing on a poroelastic medium: (a) model setup; and (b) time-load function. Note: $T_v = 1$ corresponds to 4680 d.
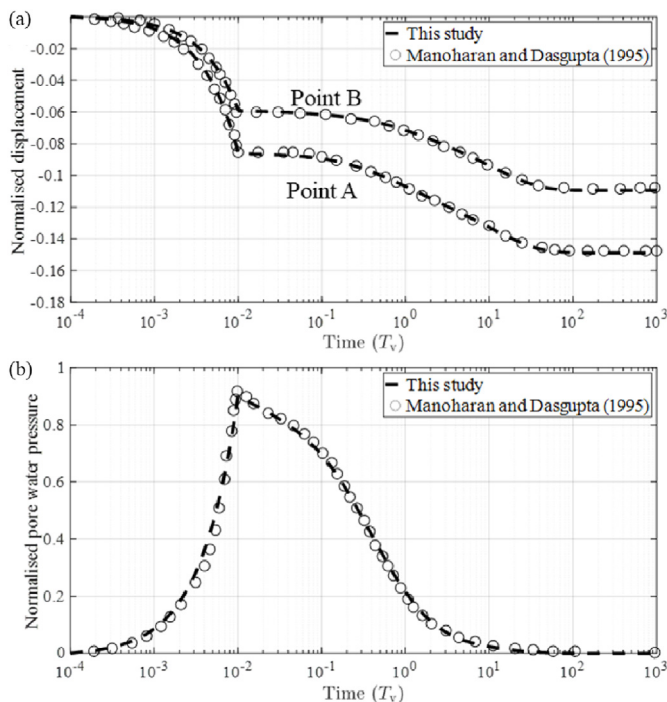

Fig. 7. Numerical results of strip footing on poroelastic medium compared with those of Manoharan and Dasgupta (1995): (a) normalised displacement at points A and B; and (b) normalised pressure at point A.

$n = 0.33$, Young's modulus $E = 2$ MPa, Poisson's ratio $\nu = 0.3$ and the Darcy hydraulic conductivity $k = 10^{-5}$ m/d. Gravity effects are not included.

To facilitate the analysis, a scaled value of time, T_v, is introduced, where $T_v = 1$ corresponds to 4680 d. The load with a width of 3 m is applied at the top surface and described by a ramp function over a period of $0.01T_v$ and then is kept constant, as depicted in Fig. 6b. The simulation is conducted for a duration of $1000T_v$, and it consists of two stages (Yuan et al., 2023b): the first loading stage (from $t = 0$ to $t = 0.01T_v$) is simulated using 100 constant time steps, while the long-term consolidation stage extends until $t = 1000T_v$ with a constantly increased time step Δt by a factor of 1.1 at each step.

Following the work of Manoharan and Dasgupta (1995), the displacements are normalised concerning the width of the load W_f, and pore water pressure is normalised concerning the maximum value of the load, i.e. 100 kPa. Fig. 7a illustrates the simulation results for the elastic behaviour of the saturated porous media. It shows that Points A and B experience rapid settlement during the loading phase ($t \leq 0.01T_v$), followed by gradual deformation due to consolidation ($0.01T_v \leq t \leq 100T_v$), and finally reach a steady state after complete dissipation of pore water pressure ($t \geq 100T_v$). The normalised displacements at points A and B agree well with the independent numerical results reported by Manoharan and Dasgupta (1995). Additionally, the normalised pore water pressure recorded at point B is nearly consistent with the results reported by Manoharan and Dasgupta (1995), as shown in Fig. 7b. The results of Yuan et al. (2023b) are not presented in this figure since they exhibit a high degree of similarity to the curves depicted in Fig. 7a and b.
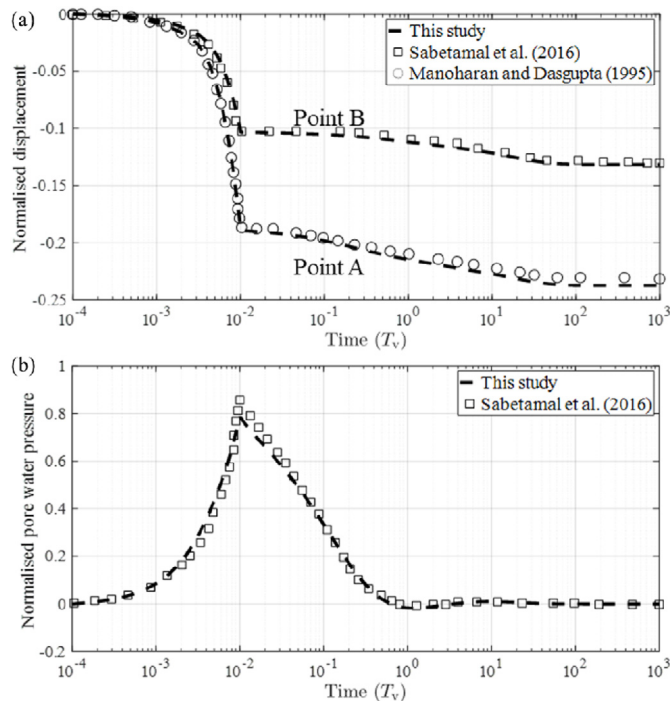
Fig. 8. Strip footing: (a) normalised displacements at points A and B compared with the results of Manoharan and Dasgupta (1995) and Sabetamal et al. (2016) for elastoplastic case; and (b) normalised pore water pressure at point B compared with the results of Sabetamal et al. (2016) for elastoplastic case.

The same numerical configuration with an elastoplastic medium is further examined. The associated Mohr-Coulomb yield criterion, with cohesion $c = 10$ kPa and friction angle $\varphi = 20°$, is adopted in this simulation which is in line with that reported by Sabetamal et al. (2016). The normalised displacement records at points A and B and normalised pore water pressure records at point A are presented in Fig. 8a and b, respectively. These results exhibit a high level of agreement with the results of Manoharan and Dasgupta (1995) and Sabetamal et al. (2016).

To demonstrate the accuracy of our model, we present the pore water pressure fields at two specific instants: $t = 0.001T_v$ and $0.01T_v$, which have been previously studied in two separate versions of smoothed PFEM (Jin et al., 2021b; Yuan et al., 2023b). In Fig. 9, numerical results are compared with those obtained from the smoothed PFEM without and with stabilisation techniques (Jin et al., 2021b; Yuan et al., 2023b). The numerical solutions from the present model at the two instants for both elastic and elastoplastic analyses are shown in Fig. 9a–d and g. These results exhibit smoother distributions compared to jagged patterns obtained by the smoothed PFEM without stabilisation techniques (i.e. Fig. 9b–e and h) (Jin et al., 2021b; Yuan et al., 2023b). Notably, when comparing Fig. 9b with Fig. 9e and h, spurious oscillations are more pronounced in the elastoplastic analysis for the smoothed PFEM without stabilisation techniques. In contrast, the present model accurately captures the realistic pore water pressure field for both elastic and elastoplastic analyses, similar to the results obtained in the smoothed PFEM with stabilisation techniques (Jin et al., 2021b; Yuan et al., 2023b) as shown in Fig. 9c–f and i, demonstrating the numerical stability of our model for elastic and elastoplastic analyses of saturated media.

3.3. Self-weight consolidation

In this section, the elastic behaviour of a saturated medium under large deformation is investigated by considering a 2D self-weight consolidation of a block. This configuration has been previously studied as a standard benchmark (Zhao and Choo, 2020; Zheng et al., 2021; Yuan et al., 2022). The elastic block is a rectangle with a width of 4 m and a height of 2 m. Due to symmetry, a square with dimensions of 2 m is adopted in the simulation. The model setup, depicted in Fig. 10a, illustrates the mesh configuration and boundary conditions. The material parameters used in the work of Zheng et al. (2021) are adopted in this study: the density of solid $\rho_s = 2650$ kg/m^3, the density of fluid $\rho_f = 1000$ kg/m^3, the porosity $n = 0.4$, the Young's modulus $E = 100$ kPa, the Poisson's ratio $\nu = 0.3$, and the Darcy hydraulic conductivity $k = 10^{-4}$ m/s. The gravity acceleration $g = 10$ m/s^2 is applied using a ramp function over a period of 0.1 s and kept as a constant, as shown in Fig. 10b. A
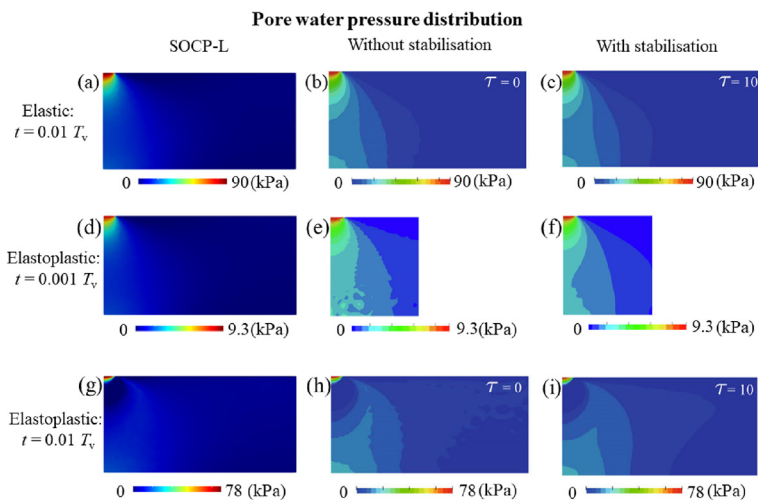

Fig. 9. Numerical results of pore water pressure obtained in this study and those by two versions of smoothed PFEM (Jin et al., 2021b; Yuan et al., 2023b): (a) elastic analysis at $t = 0.01T_v$ from this study; (b) elastic analysis without stabilisation at $t = 0.01T_v$ from the study of Yuan et al. (2023b); (c) elastic analysis with stabilisation at $t = 0.01T_v$ from the study of Yuan et al. (2023b); (d) elastoplastic analysis at $t = 0.001T_v$ from this study; (e) elastoplastic analysis without stabilisation at $t = 0.001T_v$ conducted by Jin et al. (2021b); (f) elastoplastic analysis with stabilisation at $t = 0.001T_v$ conducted by Jin et al. (2021b); (g) elastoplastic analysis at $t = 0.01T_v$ from this study; (h) elastoplastic analysis without stabilisation at $t = 0.01T_v$ conducted by Yuan et al. (2023b); and (i) elastoplastic analysis with stabilisation at $t = 0.01T_v$ conducted by Yuan et al. (2023b).
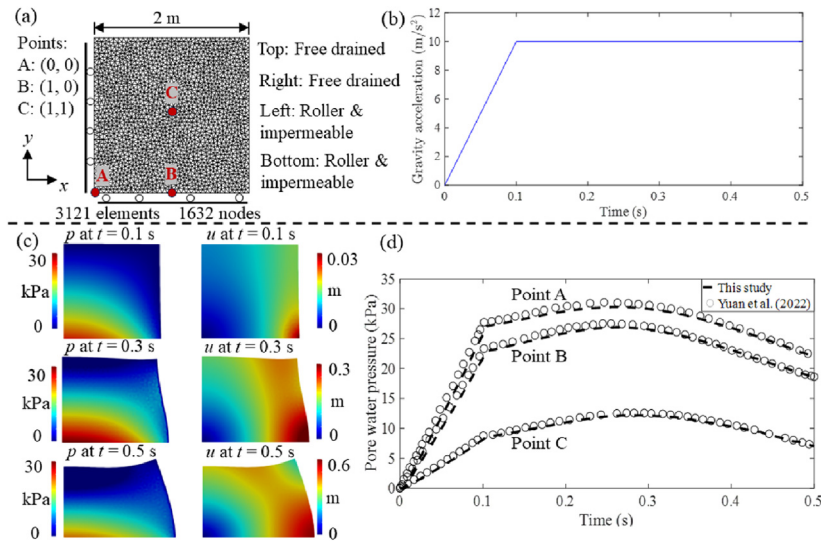
Fig. 10. 2D self-weight consolidation: (a) model setup; (b) evolution of gravity acceleration; (c) contours of pore water pressure p and the magnitude of displacement u at different instants; and (d) time history of pore water pressure at points A, B and C, compared with those in the work of Yuan et al. (2022).

constant time step of 0.005 s is used in this simulation for a duration of 0.5 s.

The numerical results of pore water pressure at three time instants, i.e. $t = 0.1$ s, 0.3 s and 0.5 s, along with the displacement at $t = 0.5$ s, are presented in Fig. 10c. Similar results have been observed in previous studies (Zheng et al., 2021, 2022; Yuan et al., 2022), where stabilisation techniques or a fractional step scheme were employed to ensure accuracy. The pore water pressure at three monitoring points, denoted as A, B, and C (as illustrated in Fig. 10a), is compared with the results of Yuan et al. (2022). Remarkably, these comparisons give good agreements, which demonstrate the validity and accuracy of our model for elastic analysis of saturated media under large deformation.

3.4. Vertical cut of a saturated soil block

In this section, a typical example of a poro-elastoplastic medium involving large deformation (Sanavia et al., 2002; Navas et al., 2018) is analysed to validate the capability of the proposed model in handling practical geotechnical problems. The model setup of a
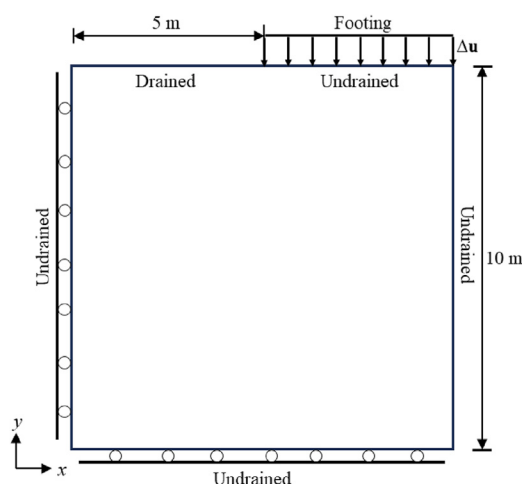

Fig. 11. Model setup for the vertical cut of a saturated soil block.

Table 1
Model parameters adopted in this study.

Parameter	Value
Density of solid, ρ_s (kg/m³)	2700
Density of fluid, ρ_f (kg/m³)	1000
Porosity, n	0.33
Young's modulus, E (MPa)	9.175
Poisson's ratio, ν	0.316
Darcy hydraulic conductivity, k (m/s)	10^{-4}
Cohesion, c (kPa)	100
Friction angle, φ (°)	20
Dilation angle, ψ (°)	0

rigid footing on a square domain of saturated soil, same as that studied by Navas et al. (2018), is shown in Fig. 11. The model parameters are shown in Table 1.

The computational domain is discretised into 31,008 linear triangular elements with 15,758 nodes, such that the total number of cells is 15,758. In the study of Navas et al. (2018), a total vertical displacement of 2 m is imposed on the loading area at a constant rate of 0.02 m/s. In this study, the load is enforced through an incremental vertical displacement of $\Delta u_y = -0.02$ m with a time step of $\Delta t = 1$ s, resulting in 100 simulation steps.

The computed pore water pressure field at two instants, $t = 50$ s and $t = 100$ s are first compared with available results. Yuan et al. (2023b) employed different values of the stabilisation parameter τ to define a stabilising term that is added to the equilibrium equation of fluid mass, to investigate the performance of a developed Polynomial-Pressure-Projection technique in stabilising the pore water pressure field in this challenging example. Since this problem involves large deformation elastoplastic analysis, the spurious oscillations in pore water pressure field are more pronounced compared to both large deformation elastic analysis and small deformation elastoplastic analysis. To alleviate this issue, a large stabilisation parameter $\tau = 100$ was used by Yuan et al. (2023b). It should be noted that a different value of stabilisation parameter 10 is used by Yuan et al. (2023b) to stabilise the numerical solution to the problem shown in Section 3.2. While the present N-PFEM model can capture the smooth distributions of field variables without using any stabilisation techniques.
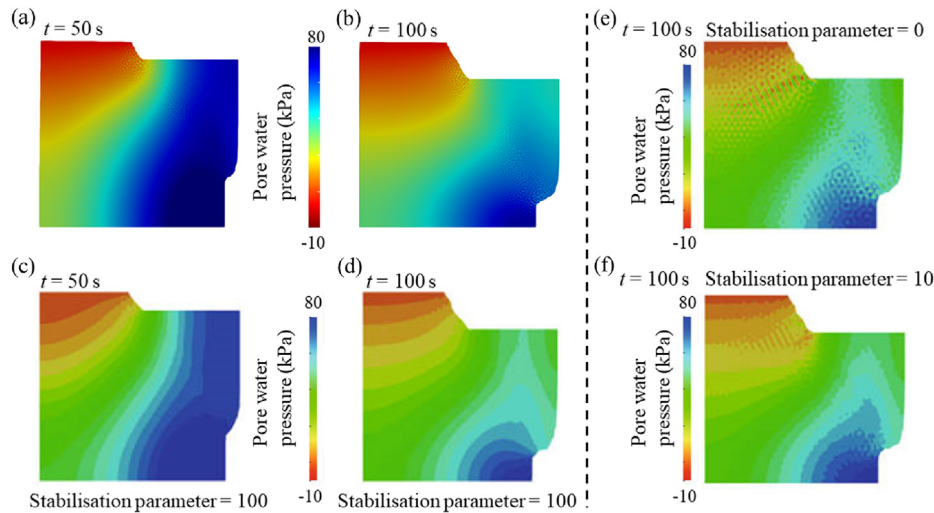
Fig. 12. Numerical solutions of pore water pressure: (a) at $t = 50$ s from this study; (b) at $t = 100$ s from this study; (c) at $t = 50$ s from the smoothed PFEM with a stabilisation parameter of 100; (d) at $t = 100$ s from the smoothed PFEM with a stabilisation parameter of 100; (e) at $t = 100$ s from the smoothed PFEM without stabilisation (the stabilisation parameter is set at 0); and (f) at $t = 100$ s from the smoothed PFEM with a stabilisation parameter of 10. (c–f) are from the work of Yuan et al. (2023b).
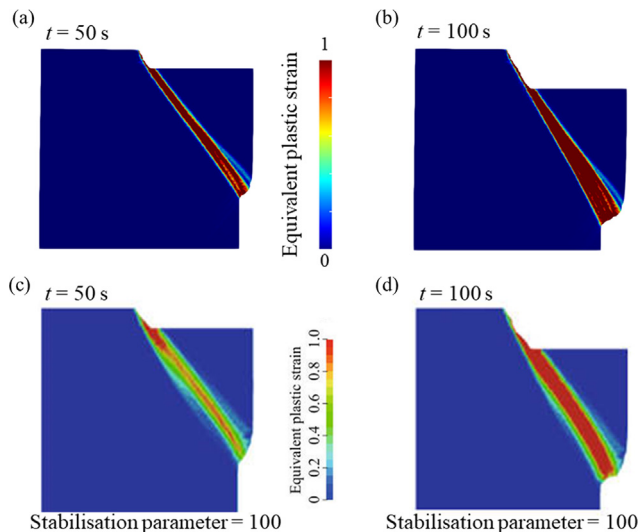

Fig. 13. Numerical solutions of equivalent plastic strain at $t = 50$ s and $t = 100$ s: (a) $t = 50$ s from this study; (b) $t = 100$ s from this study; (c) $t = 50$ s from the smoothed PFEM with a stabilisation parameter of 100 (Yuan et al., 2023b); and (d) $t = 100$ s from the smoothed PFEM with a stabilisation parameter of 100 (Yuan et al., 2023b).

The distributions of pore water pressure calculated from the N-PFEM at $t = 50$ s and $t = 100$ s are on a deformed mesh in Fig. 12a and b, which agree well with the solution from a smoothed PFEM model using a stabilisation parameter of 100 shown in Fig. 12c and d (Yuan et al., 2023b). However, due to the involvement of large deformations, a slightly jagged distribution can still be observed. This can be further improved by increasing the level of discretisation as suggested by Navas et al. (2018). To illustrate the challenges in capturing stabilised pore water pressure, the computed pore water pressure fields at $t = 100$ s obtained using the smoothed PFEM without stabilisation (i.e. the stabilisation parameter is set at 0) and with a stabilisation parameter of 10 are plotted in Fig. 12e and f, respectively (Yuan et al., 2023b). These results highlight the advantage of the proposed nodal integration-based method, since no stabilisation techniques are required when using linear triangular elements.

The calculated equivalent plastic strains at $t = 50$ s and $t = 100$ s are also illustrated in Fig. 13a and b, respectively. The captured shear bands are similar to the ones (Fig. 13c and d) observed by Yuan et al. (2023b) using the smoothed PFEM with a stabilisation parameter of 100. The deformed configurations in Fig. 13 depict the accumulation of plastic strain in narrow zones due to the slip of one part of soil on the other, which has also been reported in the work of Navas et al. (2018) and Sanavia et al. (2002). The present results support the validity of our model for large deformation elasto-plastic analysis of typical geotechnical problems.

4. Conclusions

To develop an efficient and robust PFEM framework for dynamic analysis of saturated media in the context of geotechnical engineering applications, a novel nodal integration-based approach called N-PFEM is proposed. This framework incorporates a nodal integration technique into a generalised HR variational principle-derived implicit PFEM formulation. By utilising low-order elements with a strain smoothing technique, the model can significantly reduce the computational cost and eliminate the volumetric locking issue. Additionally, tedious mapping operations after re-meshing in the original PFEM are avoided, as all field variables are evaluated at mesh nodes and nodal integrations are performed over cells.

It is demonstrated that the proposed HR variational principle-derived formulation resolves the instability issues observed in nodal-based mesh-free methods and other nodal integration-based PFEM formulations for dynamic saturated soils without the need for *ad-hoc* stabilisation techniques. The model is validated against a series of benchmark problems, exhibiting excellent agreement with reference solutions. Our work provides a valuable reference for the development of advanced numerical tools capable of simulating geotechnical applications involving large deformation and saturated conditions.

Declaration of competing interest

The authors declare that they have no known competing financial interests or personal relationships that could have appeared to influence the work reported in this paper.

Acknowledgments

Appendix A. Supplementary data

Supplementary data to this article can be found online at https://doi.org/10.1016/j.jrmge.2023.11.016.

References

Bandara, S., Soga, K., 2015. Coupling of soil deformation and pore fluid flow using material point method. Comput. Geotech. 63, 199–214.

Belytschko, T., Guo, Y., Liu, W.K., Xiao, S.P., 2000. A unified stability analysis of meshless particle methods. Int. J. Numer. Methods Eng. 48, 1359–1400.

Berti, M., Simoni, A., 2005. Experimental evidences and numerical modelling of debris flow initiated by channel runoff. Landslides 2, 171–182.

Bjerrum, L., 1967. Engineering geology of Norwegian normally-consolidated marine clays as related to settlements of buildings. Geotechnique 17, 81–118.

Bui, H.H., Nguyen, G.D., 2017. A coupled fluid-solid SPH approach to modelling flow through deformable porous media. Int. J. Solids Struct. 125, 244–264.

Cante, J., Dávalos, C., Hernández, J.A., Oliver, J., Jonsén, P., Gustafsson, G., Häggblad, H., 2014. PFEM-based modeling of industrial granular flows. Comput. Part. Mech. 1, 47–70.

Carbonell, J.M., Monforte, L., Ciantia, M.O., Arroyo, M., Gens, A., 2022. Geotechnical particle finite element method for modeling of soil-structure interaction under large deformation conditions. J. Rock Mech. Geotech. Eng. 14, 967–983.

Chen, J.S., Wu, C.T., Yoon, S., You, Y., 2001. Stabilized conforming nodal integration for Galerkin mesh-free methods. Int. J. Numer. Methods Eng. 50, 435–466.

Cremonesi, M., Frangi, A., Perego, U., 2010. A Lagrangian finite element approach for the analysis of fluid–structure interaction problems. Int. J. Numer. Methods Eng. 84, 610–630.

Cremonesi, M., Frangi, A., Perego, U., 2011. A Lagrangian finite element approach for the simulation of water-waves induced by landslides. Comput. Struct. 89, 1086–1093.

De Boer, R., 2012. Theory of Porous Media: Highlights in Historical Development and Current State. Springer Science & Business Media.

Drew, D.A., 1983. Mathematical modeling of two-phase flow. Annu. Rev. Fluid Mech. 15, 261–291.

Edelsbrunner, H., Mücke, E.P., 1994. Three-dimensional alpha shapes. ACM Trans. Graph. 13, 43–72.

Franco, B., Bathe, K.J., 1990. A discourse on the stability conditions for mixed finite element formulations. Comput. Methods Appl. Mech. Eng. 82, 27–57.

Hu, Y., Randolph, M.F., 1998. A practical numerical approach for large deformation problems in soil. Int. J. Numer. Anal. Methods GeoMech. 22, 327–350.

Iverson, R.M., Reid, M.E., LaHusen, R.G., 1997. Debris-flow mobilization from landslides. Annu. Rev. Earth Planet Sci. 25, 85–138.

Jin, Y.F., Yin, Z.Y., Zhou, X.W., Liu, F.T., 2021a. A stable node-based smoothed PFEM for solving geotechnical large deformation 2D problems. Comput. Methods Appl. Mech. Eng. 387, 114179.

Jin, Y.F., Yin, Z.Y., Li, J., Dai, J.G., 2021b. A novel implicit coupled hydro-mechanical SPFEM approach for modelling of delayed failure of cut slope in soft sensitive clay. Comput. Geotech. 140, 104474.

Jin, Y.F., Yin, Z.Y., 2022. Two-phase PFEM with stable nodal integration for large deformation hydromechanical coupled geotechnical problems. Comput. Methods Appl. Mech. Eng. 392, 114660.

Kong, D., Martin, C.M., Byrne, B.W., 2018. Sequential limit analysis of pipe-soil interaction during large-amplitude cyclic lateral displacements. Geotechnique 68, 64–75.

Kularathna, S., Liang, W., Zhao, T., Chandra, B., Zhao, J., Soga, K., 2021. A semi-implicit material point method based on fractional-step method for saturated soil. Int. J. Numer. Anal. Methods GeoMech. 45, 1405–1436.

Lian, Y., Bui, H.H., Nguyen, G.D., Haque, A., 2023. An effective and stabilised (u–p_l) SPH framework for large deformation and failure analysis of saturated porous media. Comput. Methods Appl. Mech. Eng. 408, 1–33.

Liu, G.R., Dai, K.Y., Nguyen, T.T., 2007. A smoothed finite element method for mechanics problems. Comput. Mech. 39, 859–877.

Manoharan, N., Dasgupta, S.P., 1995. Consolidation analysis of elasto-plastic soil. Comput. Struct. 54, 1005–1021.

Markert, B., Heider, Y., Ehlers, W., 2010. Comparison of monolithic and splitting solution schemes for dynamic porous media problems. Int. J. Numer. Methods Eng. 1341–1383.

Meduri, S., Cremonesi, M., Perego, U., 2019. An efficient runtime mesh smoothing technique for 3D explicit Lagrangian free-surface fluid flow simulations. Int. J. Numer. Methods Eng. 117, 430–452.

Meng, J., Zhang, X., Huang, J., Tang, H., Mattsson, H., Laue, J., 2020. A smoothed finite element method using second-order cone programming. Comput. Geotech. 123, 103547.

Monforte, L., Navas, P., Carbonell, J.M., Arroyo, M., Gens, A., 2019. Low-order stabilized finite element for the full Biot formulation in soil mechanics at finite strain. Int. J. Numer. Anal. Methods GeoMech. 43, 1488–1515.

Navas, P., Sanavia, L., López-Querol, S., Yu, R.C., 2018. Explicit meshfree solution for large deformation dynamic problems in saturated porous media. Acta Geotech 13, 227–242.

Olson, R.E., 1998. Settlement analysis of embankments on soft clays. J. Geotech. Geoenvironmental Eng. 124, 659–669.

Oñate, E., Idelsohn, S.R., Del Pin, F., Aubry, R., 2004. The particle finite element method-an overview. Int. J. Comput. Methods 1, 267–307.

Pastor, M., Haddad, B., Sorbino, G., Cuomo, S., Drempetic, V., 2009. A depth-integrated, coupled SPH model for flow-like landslides and related phenomena. Int. J. Numer. Anal. Methods GeoMech. 33, 143–172.

Peng, C., Xu, G., Wu, W., Yu, H. sui, Wang, C., 2017. Multiphase SPH modeling of free surface flow in porous media with variable porosity. Comput. Geotech. 81, 239–248.

Prevost, J.H., 1983. Implicit-explicit schemes for nonlinear consolidation. Comput. Methods Appl. Mech. Eng. 39, 225–239.

Puso, M.A., Chen, J.S., Zywicz, E., Elmer, W., 2008. Meshfree and finite element nodal integration methods. Int. J. Numer. Methods Eng. 74, 416–446.

Reddy, J.N., 2002. Energy Principles and Variational Methods in Applied Mechanics. John Wiley & Sons.

Sabetamal, H., Nazem, M., Carter, J.P., Sloan, S.W., 2014. Large deformation dynamic analysis of saturated porous media with applications to penetration problems. Comput. Geotech. 55, 117–131.

Sabetamal, H., Nazem, M., Sloan, S.W., Carter, J.P., 2016. Frictionless contact formulation for dynamic analysis of nonlinear saturated porous media based on the mortar method. Int. J. Numer. Anal. Methods GeoMech. 40, 25–61.

Sanavia, L., Schrefler, B.A., Steinmann, P., 2002. A formulation for an unsaturated porous medium undergoing large inelastic strains. Comput. Mech. 28, 137–151.

Silva-Valenzuela, R., Ortiz-Bernardin, A., Sukumar, N., Artioli, E., Hitschfeld-Kahler, N., 2020. A nodal integration scheme for meshfree Galerkin methods using the virtual element decomposition. Int. J. Numer. Methods Eng. 121, 2174–2205.

Tian, Y., Cassidy, M.J., Randolph, M.F., Wang, D., Gaudin, C., 2014. A simple implementation of RITSS and its application in large deformation analysis. Comput. Geotech. 56, 160–167.

Torres, R., Dietrich, W.E., Montgomery, D.R., Anderson, S.P., Loague, K., 1998. Unsaturated zone processes and the hydrologic response of a steep, unchanneled catchment. Water Resour. Res. 34, 1865–1879.

Wang, D., Bienen, B., Nazem, M., Tian, Y., Zheng, J., Pucker, T., Randolph, M.F., 2015. Large deformation finite element analyses in geotechnical engineering. Comput. Geotech. 65, 104–114.

Wang, L., Zhang, X., Zhang, S., Tinti, S., 2021a. A generalized Hellinger-Reissner variational principle and its PFEM formulation for dynamic analysis of saturated porous media. Comput. Geotech. 132, 103994.

Wang, L., Zhang, X., Zaniboni, F., Oñate, E., Tinti, S., 2021b. Mathematical optimization problems for particle finite element analysis applied to 2D landslide modeling. Math. Geosci. 53, 81–103.

Wang, L., Zhang, X., Lei, Q., Panayides, S., Tinti, S., 2022. A three-dimensional particle finite element model for simulating soil flow with elastoplasticity. Acta Geotech 17, 5639–5653.

Wang, L., Lei, Q., 2023. Modelling the pre- and post-failure behaviour of faulted rock slopes based on the particle finite element method with a damage mechanics model. Comput. Geotech. 153, 105057.

Wang, Z., Jin, Y., Yin, Z., Wang, Y., 2023a. A dynamic SNS-PFEM with generalized-α method for hydro-mechanical coupled geotechnical problems. Comput. Geotech. 159, 105466.

Wang, L., Zhang, X., Tinti, S., 2023b. Formulation for wave propagation in dissipative media and its application to absorbing layers in elastoplastic analysis using mathematical programming. Int. J. Numer. Methods Eng. 124, 3387-345.

Wang, L., Zhang, X., Geng, X., Lei, Q., 2023c. Nodal integration-based particle finite element method (N-PFEM) for poro-elastoplastic modelling of saturated soils under large deformation. Comput. Geotech. 161, 105567.

Wei, H., Chen, J.-S., Beckwith, F., Baek, J., 2020. A naturally stabilized semi-Lagrangian meshfree formulation for multiphase porous media with application to landslide modeling. J. Eng. Mech. 146, 04020012.

Wood, W.L., 1990. Practical Time-Stepping Schemes. Oxford University Press, UK.

Yamaguchi, Y., Takase, S., Moriguchi, S., Terada, K., 2020. Solid–liquid coupled material point method for simulation of ground collapse with fluidization. Comput. Part. Mech. 7, 209–223.

Yuan, W.H., Wang, B., Zhang, W., Jiang, Q., Feng, X.T., 2019. Development of an explicit smoothed particle finite element method for geotechnical applications. Comput. Geotech. 106, 42–51.

Yuan, W.H., Zhu, J.X., Liu, K., Zhang, W., Dai, B.B., Wang, Y., 2022. Dynamic analysis of large deformation problems in saturated porous media by smoothed particle finite element method. Comput. Methods Appl. Mech. Eng. 392, 114724.

Yuan, W.H., Liu, M., Guo, N., Dai, B.B., Zhang, W., Wang, Y., 2023a. A temporal stable smoothed particle finite element method for large deformation problems in geomechanics. Comput. Geotech. 156.

Yuan, W.H., Liu, M., Zhang, X.W., Wang, H.L., Zhang, W., Wu, W., 2023b. Stabilized smoothed particle finite element method for coupled large deformation problems in geotechnics. Acta Geotech 18, 1215–1231.

Zeng, W., Liu, G.R., 2018. Smoothed finite element methods (S-FEM): an overview and recent developments. Arch. Comput. Methods Eng. 25, 397−435.

Zhang, H.W., Wang, K.P., Chen, Z., 2009. Material point method for dynamic analysis of saturated porous media under external contact/impact of solid bodies. Comput. Methods Appl. Mech. Eng. 198, 1456−1472.

Zhang, Z.Q., Liu, G.R., 2010. Temporal stabilization of the node-based smoothed finite element method and solution bound of linear elastostatics and vibration problems. Comput. Mech. 46, 229−246.

Zhang, X., Krabbenhoft, K., Pedroso, D.M., Lyamin, A.V., Sheng, D., Vicente da Silva, M., Wang, D., 2013. Particle finite element analysis of large deformation and granular flow problems. Comput. Geotech. 54, 133−142.

Zhang, X., Krabbenhoft, K., Sheng, D., 2014. Particle finite element analysis of the granular column collapse problem. Granul. Matter 16, 609−619.

Zhang, X., Sheng, D., Sloan, S.W., Krabbenhoft, K., 2016. Second-order cone programming formulation for consolidation analysis of saturated porous media. Comput. Mech. 58, 29−43.

Zhang, W., Yuan, W., Dai, B., 2018. Smoothed particle finite-element method for large-deformation problems in geomechanics. Int. J. GeoMech. 18, 04018010.

Zhang, X., Oñate, E., Torres, S.A.G., Bleyer, J., Krabbenhoft, K., 2019. A unified Lagrangian formulation for solid and fluid dynamics and its possibility for modelling submarine landslides and their consequences. Comput. Methods Appl. Mech. Eng. 343, 314−338.

Zhang, W., Zhong, Z., Peng, C., Yuan, W., Wu, W., 2021. GPU-accelerated smoothed particle finite element method for large deformation analysis in geomechanics. Comput. Geotech. 129, 103856.

Zhang, X., Meng, J., Yuan, S., 2022. An implicit nodal integration based PFEM for soil flow problems. Comput. Geotech. 142, 104571.

Zhang, Y., Zhang, X., Nguyen, H., Li, X., Wang, L., 2023. An implicit 3D nodal integration based PFEM (N-PFEM) of natural temporal stability for dynamic analysis of granular flow and landslide problems. Comput. Geotech. 159, 105434.

Zhao, Y., Choo, J., 2020. Stabilized material point methods for coupled large deformation and fluid flow in porous materials. Comput. Methods Appl. Mech. Eng. 362, 112742.

Zheng, X., Pisanò, F., Vardon, P.J., Hicks, M.A., 2021. An explicit stabilised material point method for coupled hydromechanical problems in two-phase porous media. Comput. Geotech. 135.

Zheng, X., Pisanò, F., Vardon, P.J., Hicks, M.A., 2022. Fully implicit, stabilised, three-field material point method for dynamic coupled problems. Eng. Comput. 38, 5583−5602.

Zienkiewicz, O.C., Chang, C.T., Bettess, P., 1980. Drained, undrained, consolidating and dynamic behaviour assumptions in soils. Geotechnique 30, 385−395.

Zienkiewicz, O.C., Shiomi, T., 1984. Dynamic behaviour of saturated porous media; The generalized Biot formulation and its numerical solution. Int. J. Numer. Anal. Methods GeoMech. 8, 71−96.

Zienkiewicz, O., Chan, A., Pastor, M., Schrefler, B., Shiomi, T., 1999. Computational Geomechanics with Special Reference to Earthquake Engineering, Computational Geomechanics. John Wiley & Sons, New York, USA.

Dr. Liang Wang is a computational geoscientist and geotechnical engineer with 10 years of experience in the study of geohazards. He received his BSc (2014) and MSc (2016) degrees in Geological Engineering from Southwest Jiaotong University and in Geotechnical Engineering from Dalian University of Technology, respectively. He obtained his PhD (2020) in Geophysics from the University of Bologna, Italy. He worked for five months as a Research Fellow in the Tsunami Research Team at the University of Bologna, and then three years as a Research Scientist in Engineering Geology at ETH Zürich, Switzerland. His research aims to advance our predictive understanding of catastrophic failure in geomaterials and quantify potential extreme geohazards at different temporal and spatial scales in natural environments and engineering applications.